remote sensing

MDPI

Article

Damage Properties of the Block-Stone Embankment in the Qinghai–Tibet Highway Using Ground-Penetrating Radar Imagery

Shunshun Qi [1,2,3], Gouyu Li [1,2,3,*], Dun Chen [1,2,3,4], Mingtang Chai [5], Yu Zhou [1,2,3], Qingsong Du [1,2,3], Yapeng Cao [1,2,3], Liyun Tang [6] and Hailiang Jia [6]

1 State Key Laboratory of Frozen Soil Engineering, Northwest Institute of Eco-Environment and Resources, Chinese Academy of Sciences, Lanzhou 730000, China; qishunshun@nieer.ac.cn (S.Q.); chendun@lzb.ac.cn (D.C.); zhouyu@lzb.ac.cn (Y.Z.); xbdqs@lzb.ac.cn (Q.D.); caoyapeng@lzb.ac.cn (Y.C.)
2 University of Chinese Academy of Sciences, Beijing 100049, China
3 Da Xing'anling Observation and Research Station of Frozen-Ground Engineering and Environment, Northwest Institute of Eco-Environment and Resources, Chinese Academy of Sciences, Jagedaqi 165000, China
4 State Key Laboratory for Geomechanics and Deep Underground Engineering, China University of Mining and Technology, Xuzhou 221116, China
5 School of Civil and Hydraulic Engineering, Ningxia University, Yinchuan 750014, China; chaimingtang@nxu.edu.cn
6 School of Architecture and Civil Engineering, Xi'an University of Science and Technology, Xi'an 710064, China; tangly@xust.edu.cn (L.T.); hailiang.jia@xust.edu.cn (H.J.)
* Correspondence: guoyuli@lzb.ac.cn

Abstract: The block-stone embankment is a special type of embankment widely used to protect the stability of the underlying warm and ice-rich permafrost. Under the influence of multiple factors, certain damages will still occur in the block-stone embankment after a period of operation, which may weaken or destroy its cooling function, introducing more serious damages to the Qinghai–Tibet Highway (QTH). Ground-penetrating radar (GPR), a nondestructive testing technique, was adopted to investigate the damage properties of the damaged block-stone embankment. GPR imagery, together with the other data and methods (structural characteristics, field survey data, GPR parameters, etc.), indicated four categories of damage: (i) loosening of the upper sand-gravel layer; (ii) loosening of the block-stone layer; (iii) settlement of the block-stone layer; and (iv) dense filling of the block-stones layer. The first two conditions were widely distributed, whereas the settlement and dense filling of the block-stone layer were less so, and the other combined damages also occurred frequently. The close correlation between the different damages indicated a causal relationship. A preliminary discussion of these observations about the influences on the formation of the damage of the block-stone embankment is included. The findings provide some points of reference for the future construction and maintenance of block-stone embankments in permafrost regions.

Keywords: ground-penetrating radar; Qinghai–Tibet highway; block-stone embankment; permafrost; embankment ratios

Citation: Qi, S.; Li, G.; Chen, D.; Chai, M.; Zhou, Y.; Du, Q.; Cao, Y.; Tang, L.; Jia, H. Damage Properties of the Block-Stone Embankment in the Qinghai–Tibet Highway Using Ground-Penetrating Radar Imagery. *Remote Sens.* **2022**, *14*, 2950. https://doi.org/10.3390/rs14122950

Academic Editors: Valerio Baiocchi, Alessandro Mei and Xianfeng Zhang

Received: 3 May 2022
Accepted: 17 June 2022
Published: 20 June 2022

1. Introduction

The QTH, built in 1954, is a major artery connecting the interior of Chinese territory and the remote Qinghai–Tibet Plateau (QTP). Of its total length of 1937 km, 528.5 km is over continuous permafrost terrain [1]. Due to global warming, the permafrost table on the QTP has fallen significantly [2–4], and the presence of the QTH has modified the water and heat exchange conditions of the original soil on the QTP. This has created a surface temperature difference between the black asphalt pavement and the natural ground surface, which has accelerated the permafrost thaw under the highway embankment [5–11]. In addition, the

sunny–shady slopes effect, which means that the sunny slope (east-facing slope) of the highway embankment absorbs more solar heat and exhibits a higher surface ground temperature, has led to the asymmetry of the thaw depth in the highway embankment [12,13]. The insulation effect of snow on highway embankment slopes in winter further warms the permafrost [14]. These effects have affected the stability of the higher and ice-rich permafrost under the embankment along the QTP engineering corridor. This destabilizing effect is the main reason for embankment damages in permafrost regions, being closely related to the temperature and ice content of the permafrost [15–17]. Therefore, a large number of special highway embankments have been built in the QTH to reduce the impact of changes in the permafrost.

Two categories of special highway embankments are currently employed in the QTH: passive and proactive temperature-controlling measures [18]. The passive measures mainly rely on maintaining the current ground temperature to slow down the degradation of the permafrost, such as thermal-insulated highway embankments [19,20]. Proactive measures have been designed to actively change the thermal condition of the permafrost so that it develops in a direction that is conducive to the stability of the embankment, such as duct-ventilated embankments, block-stone embankments, and thermosyphon embankments (Figure 1) [18,21–24]. Block-stone embankments protect the underlying permafrost by changing the embankment structure and using the convective heat transfer of air in the porous block-stone layer to increase the cooling capacity of the embankment [25,26]. However, after this system has run for a certain period, various damages occur in the block-stone embankment [27], and its cooling effect is weakened or disappears. The weakening or loss of the cooling effect will produce more serious damage in this section of the highway. Studies to date have mainly focused on the design and optimization of the structure of block-stone embankments [28–32], with little research on their damages.

The QTH is used to transport materials and a large number of tourists in and out of Tibet. Therefore, its normal operation is vital to local economic development and social stability. The traditional methods, such as hammer sounding, destructive coring, and testing pits, were used to investigate the damage characteristics of the highway that would affect the normal operation of the highway [17,22]. Meanwhile, the QTP environment is harsh. The large-scale surveys are time-consuming and labor-intensive, which is a burden on the technicians and the fragile QTP environment. In the past, investigations of QTH damages mainly focused on visual inspection, supplemented by local field surveys. The highway conditions can only be generally evaluated with limited borehole data observations since it is difficult to obtain specific information about the conditions under the embankment [33].

Ground-penetrating radar (GPR) detects and characterizes underground targets using changes in the electromagnetic characteristics of the medium, and allows the continuous, large-scale, long-distance, non-destructive detection of targets. [34–36]. Therefore, GPR is widely used in geotechnical engineering, environmental protection, archeological site detection, geological research, underground pipeline detection, detection of urban public facilities, and military detection [37–46]. Based on this, GPR has more advantages in continuous long-distance highway engineering detection. For example, Solla et al. [47] reviewed the published literature to demonstrate the method, advantages, and disadvantages of GPR in highway infrastructure detection, along with up-to-date research results, and potential. Peng et al. [48] systematically expounded on the application of GPR in highway damage detection together with typical engineering examples, proved its superiority, and discussed the future development of GPR. Krysiński et al. [49] used GPR to study pavement cracks in semi-rigid highways and analyzed the characteristics of GPR signals in detail.

There are two main applications of GPR in the permafrost regions. One is to research the distribution characteristics and degradation mechanism of permafrost, and the determination of parameters related to specific strata [50–55]. The other is to research the impact of the presence and degradation of permafrost on engineering facilities (highways, railways, airports, pipelines, etc.) in these regions [56–60]. The QTH has been seriously deformed or

even damaged due to changes in the properties of the underlying permafrost. Thus, the use of GPR for QTH damage research has a very broad application potential.

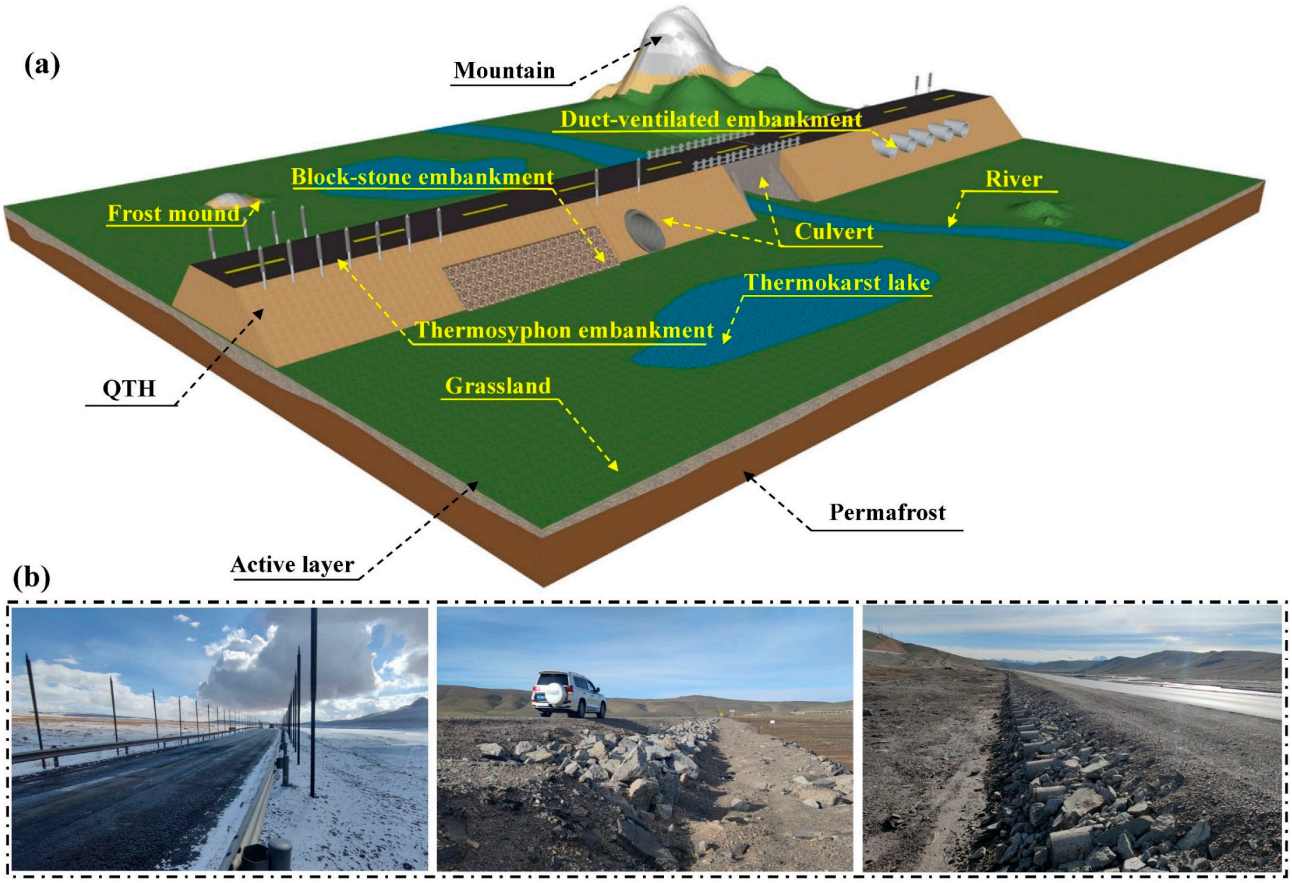

Figure 1. (**a**) Proactive temperature-controlling measures and the surrounding environment along the QTH; (**b**) field photographs, from left to right: thermosyphon embankment; block-stone embankment, and duct-ventilated embankment.

In this paper, we present a highway embankment monitoring technology based on GPR image characteristics. According to that, different damages of the block-stone embankment were identified and classified based on their GPR imagery, and the distribution and mutual relationships of different damages were investigated. Then, from the findings of the study, a preliminary discussion of the damage-causing process of the block-stone embankment is included. The research results provide references for the subsequent construction and maintenance of block-stone embankments in permafrost regions.

2. Study Area

2.1. Physical Geography of the Study Region

The permafrost on the QTP is the largest high-altitude permafrost in the world, covering an area of 1.06×10^6 km^2, and accounting for about 40.2% of the land area of the QTP [61–64]. There are many linear infrastructures such as the QTH, the Qinghai–Tibet Railway, and the Golmud–Lhasa Oil Product Pipeline. The QTH is located at an elevation of 4000–5231 m, the annual average temperature varies from −2 to −7 °C, and the annual freezing period lasts for 7–8 months. The permafrost region has poor geological conditions due to lots of periglacial phenomena (e.g., frost mounds, ice layers, and thermokarst lakes) [22,65].

The study area is the block-stone embankment section from K3024 to K3025 (Figure 2), which is located in the Kekexili Nature Reserve. The average elevation of the mountainous area is 4600–4700 m, the average annual temperature is −5.5 to −6.5 °C, the permafrost temperature is −0.5 to −1.8 °C, and the permafrost table at natural sites is 1.5–3.5 m below the ground surface [22,64]. The vegetation on both sides of the highway is sparse, and the vegetation grows at some distance from the highway.

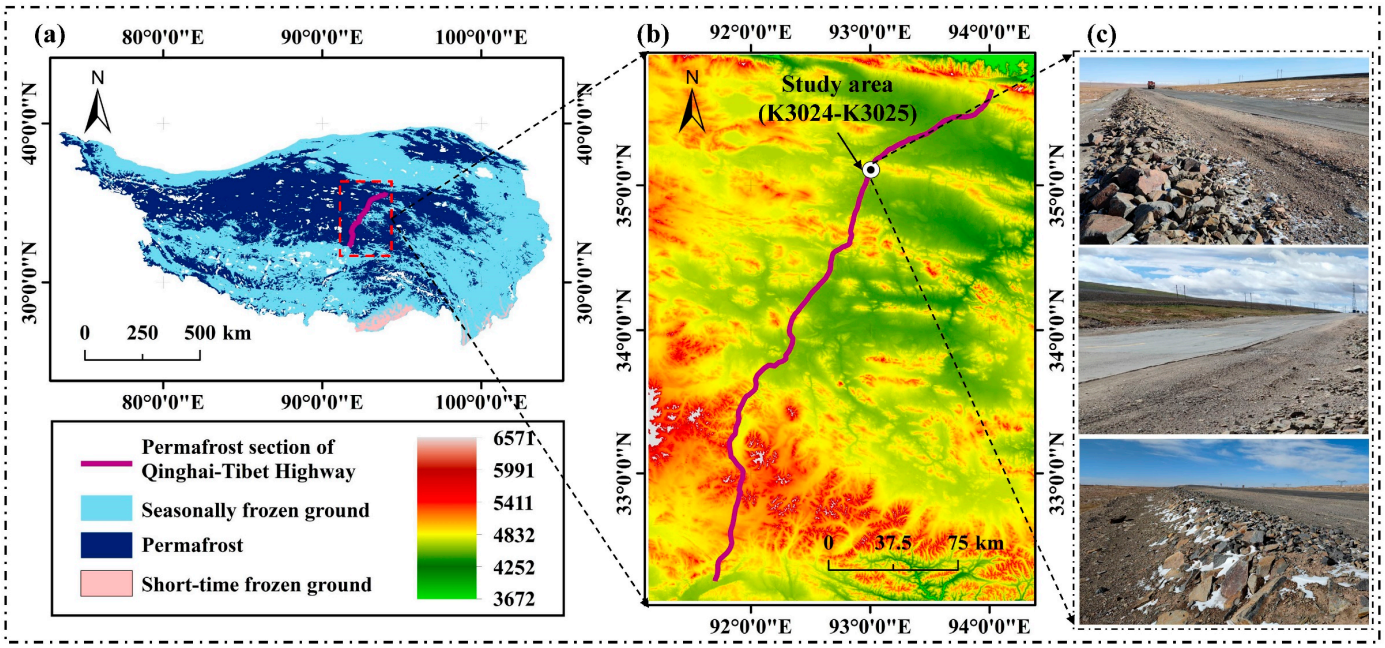

Figure 2. Study area: (**a**) spatial distribution of permafrost region in the QTP (the permafrost map is from [61,62]); (**b**) the location of k3024 to K3025 in the QTH; (**c**) field photographs of k3024 to k3025, from top to bottom: "wavy" pavement; local settlement of embankment and the block-stone embankment.

The permafrost type underlying the highway embankment in this section belongs to the icy permafrost exhibiting an ice layer with litter soil at a certain depth, classified as a sub-stable area depending on the overall stability of the entire QTH [22]. The engineering geological condition of the permafrost has been evaluated as a poor one. The overall highway in the permafrost areas is severely damaged, and the embankment has settled unevenly, with dense transverse and longitudinal cracks on the asphalt pavement. This has resulted in a "wavy" pavement as a whole and vehicle traffic ability is poor.

2.2. Block-Stone Embankment

2.2.1. The Structure and Materials of the Block-Stone Embankment

The purpose of the block-stone embankment is to reduce the temperature in the embankment by placing a layer of stone in the lower part of the highway embankment and removing the heat in the embankment in winter. Figure 3 shows the typical block-stone embankment structure. This includes the gravel layer, bottom sand-gravel layer, block-stone layer, and top sand-gravel layer from bottom to top [24,66,67].

The bottom gravel layer (general thickness 0.3–0.5 m) is in direct contact with the original ground, being densely compacted by vibration rolling. It is overlain by a layer of geotextile and sand-gravel, mainly to provide a good foundation for the block-stone layer. The overlying block-stone layer, which is the core of the block-stone embankment, is generally between 1.0 and1.5 m thick. The stone size is 150–300 mm, the porosity is not less than 25%, and the slenderness ratio is designed to be less than 3. In addition, single-layer filling and double-layer filling are selected depending on the ice content of the permafrost under the embankment. The structure shown in Figure 3 is double-layer filling.

The overlying sand-gravel layer is divided into upper and lower sand-gravel layers and is part of the auxiliary protection structure. The top sand-gravel layer (generally 0.3-m-thick) above the block-stone layer is separated by a geotextile and gravel layer. Their main function is to prevent fines from entering the block-stone layer, ensuring its convection effect. A lower 0.5-m-thick sand-gravel layer is located above the gravel layer [24,66,67].

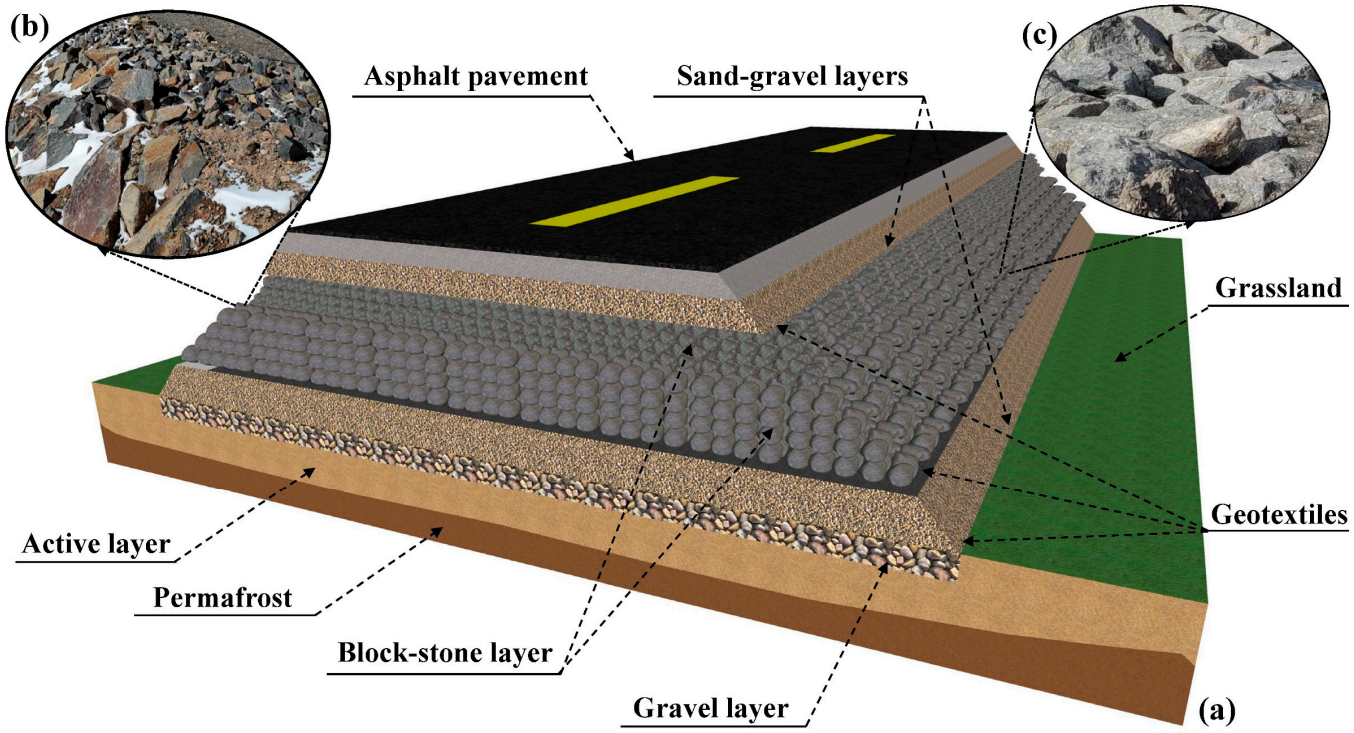

Figure 3. Schematic diagram of the block-stone embankment: (**a**) block-stone embankment structure; (**b**,**c**) field photographs of block-stone layer.

2.2.2. Working Principle of the Block-Stone Embankment

During the cold season, the cold air with a large density flows downward via the pores in the block-stone layer and the warm air rises correspondingly, causing a temperature difference by convective heat transfer, thereby removing the heat from the embankment and the active layer (Figure 4a). This cycle lowers the temperatures of the embankment and the underlying active layer and permafrost, protecting the permafrost from thaw [24,66].

During the warm season, the atmospheric heat is transferred into the embankment through the asphalt pavement and the slopes of the embankment by heat conduction, heating the air in the block-stone layer. Because the warmer air is in the upper part of the block-stone layer and the cold air is in the lower part, there is no convective heat transfer in the stone layer. The reduced heat exchange between the upper part and lower part of the block-stone layer happens only by conduction, which equivalently forms a layer of a heat insulation barrier at the bottom in summer (Figure 4b). This "thermal diode" effect takes place to cool the underlying permafrost [24,67].

2.3. Factors Leading to Block-Stone Embankment Damage

The stability of the block-stone highway embankment and the underlying permafrost is influenced by the surrounding environmental factors which may be summarized as natural or human factors.

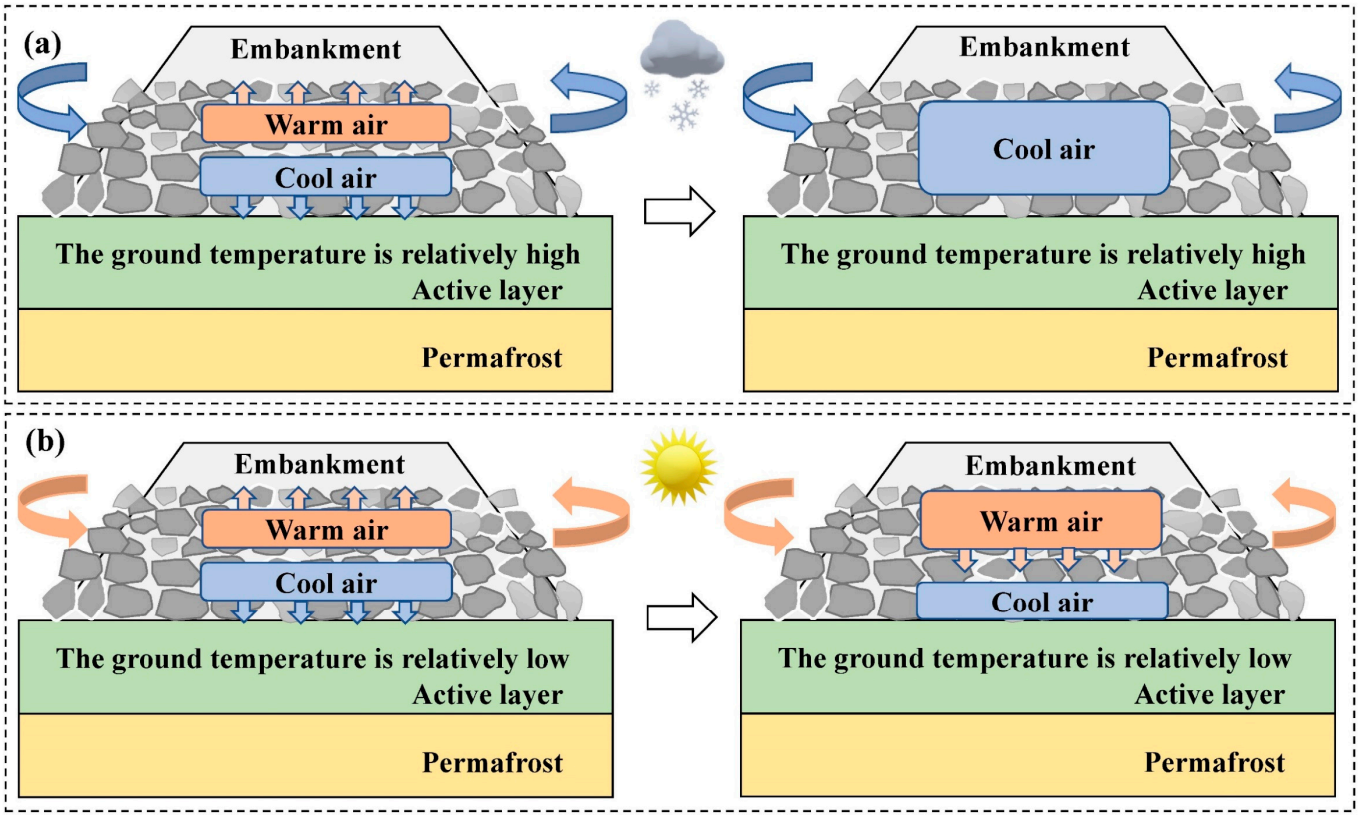

Figure 4. Schematic diagram of the working principle of a block-stone embankment: (**a**) cold season; (**b**) warm season.

2.3.1. Natural Factors

Natural factors are the main reasons for damages in block-stone embankments. They are climatic conditions and the properties of the underlying permafrost.

The natural environment on the QTP is harsh with a cold and dry climate, a freezing period for 7–8 months a year, strong solar radiation, unevenly distributed precipitation, and strong winds. This harsh environment causes severe damage to the highway, greatly reducing its service life [22,66]. In addition, the strong wind has a weathering effect on the block-stone layer, reducing the strength of the block-stones themselves and warming the permafrost under the embankment [27]. Moreover, the high ground temperature and ice content of the underlying permafrost are the main factors controlling the stability of highway embankments. Additionally, the sunny–shady effect along the QTH is another important factor leading to embankment damage [13].

2.3.2. Human Factors

Human factors, mainly including engineering construction, vehicle driving, and highway maintenance and replacement, are also important factors influencing the stability of the block-stone embankment.

Human activities destroy the thermal balance of the original ground, change the environmental and engineering geological conditions of the permafrost, and decrease the stability of the embankment [5–11]. In addition, the construction quality also affects the service life of the block-stone embankment to a great extent [24]. The traffic vehicles on the QTH are mainly heavy trucks whose long-term rolling and frequent braking lead to severe damage to the highway. Because of the harsh natural environment, highway maintenance is not immediate, which leads to gradual damage development.

3. Data and Methods

3.1. Working Principle of GPR

GPR is a geophysical method of detecting underground mediums by the reflection and refraction of electromagnetic waves in the medium [34–36]. Figure 5 shows the classical GPR process for detecting subsurface targets. The electromagnetic waves emitted by the transmitting antenna are reflected by the layers under the highway and then return to the receiving antenna (Figure 5b). The two-way travel time t of the electromagnetic wave is calculated from

$$t = \frac{\sqrt{4h^2 + x^2}}{v} \tag{1}$$

where h is the depth of the target (m) and x is the offset between the transmitting antenna and the receiving antenna (m). When the transmitting and receiving antenna are shielded, x is ignored. v is the velocity of electromagnetic wave propagation in the medium, which is given by

$$v = \frac{C}{\sqrt{\varepsilon}} \tag{2}$$

where C is the propagation velocity in free space (3×10^8 m/s) and ε is the dielectric constant of the medium. Therefore, the buried depth of the target can be calculated if the two-way travel time and dielectric constant are known. The use of this method can accurately calculate the depth of, for example, underground pipes, wires, and tombs [37,41,42], etc. The dielectric constant can be calculated if the buried depth of the target and the two-way travel time of the electromagnetic wave is known [68]. This method is mostly used in practice to estimate the dielectric constant of the mixture of actual surveys; for example, the dielectric constant of permafrost and active layer calculated by this method can inversely deduce the ice content of permafrost and the water content of the active layer [50,54,55,57].

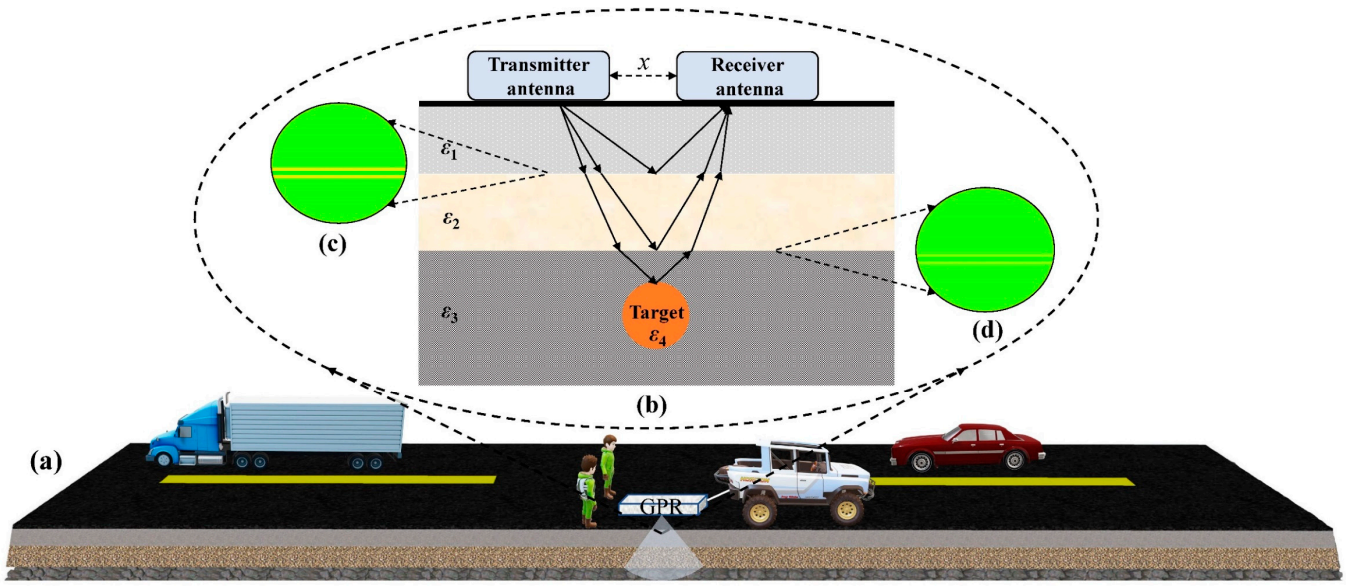

Figure 5. Schematic diagram of the GPR survey on the highway: (**a**) highway; (**b**) the electromagnetic waves emitted by the transmitting antenna are reflected by the different layers and then return to the receiving antenna; (**c**) strong electromagnetic wave reflection; (**d**) weak electromagnetic wave reflection.

In addition, the frequency for GPR detection should be selected in combination with the actual situation: a low-frequency signal has a deeper penetration but a poorer resolution, and a high-frequency antenna gives a shallower penetration depth and a better resolu-

tion [37]. At present, the GPR of many companies shield two sets of antennas with different frequencies, which can meet the requirements of depth and accuracy at the same time.

3.2. Data Acquisition

With the financial support of a Chinese research project, named the Second Tibetan Plateau Scientific and Research Expedition, XPRT Crossover CO730 two-dimensional GPR (Impulse Radar, Sweden) was used to conduct a field survey in the whole permafrost section of the QTH in October 2020 (Figure 6). This GPR system shielded antennae with frequencies centered around 70 and 300 MHz to measure different depths at different precisions. The GPR parameter settings are listed in Table 1. During the survey, the abnormal highway conditions and surrounding conditions were recorded in detail, and GPS positioning was used to locate the start and end positions of each dataset, providing references for subsequent image interpretation.

Figure 6. Diagram of the field GPR survey on QTH: (**a**) GPR survey system; (**b**) site survey.

Table 1. Parameter setting of GPR.

Parameters and Device	Setting A	Setting B
Antenna frequency (MHz)	300	70
Antenna offset (m)	0.23	0.6
Time window (ns)	93	375
Sampling rate (m)	0.05	0.05
Samples	300	300
Trigger device	Wheel	Wheel

3.3. Data Processing and Presentation

The purpose of the data processing was to suppress noise, enhance the signal, and improve the signal-to-noise ratio of the data, extracting useful information about GPR data [69].

Data processing software Reflexw (Sandmeier Geophysical Research, Karlsruhe, Germany) was used to process raw GPR data as follows (Figure 7) including 6 steps [35,70,71], i.e., input data, removing direct waves (static correction), exponential gain, 2-D filtering (average path extraction), 1-D filtering (band-pass Butterworth filtering), and 2-D filtering (moving average). The GPR data profile processing is shown in Figure 7f, and the reflection of the target horizon is clearer. In addition, the steps and methods of data processing should be adjusted according to the requirements of image interpretation to achieve the best processing effect.

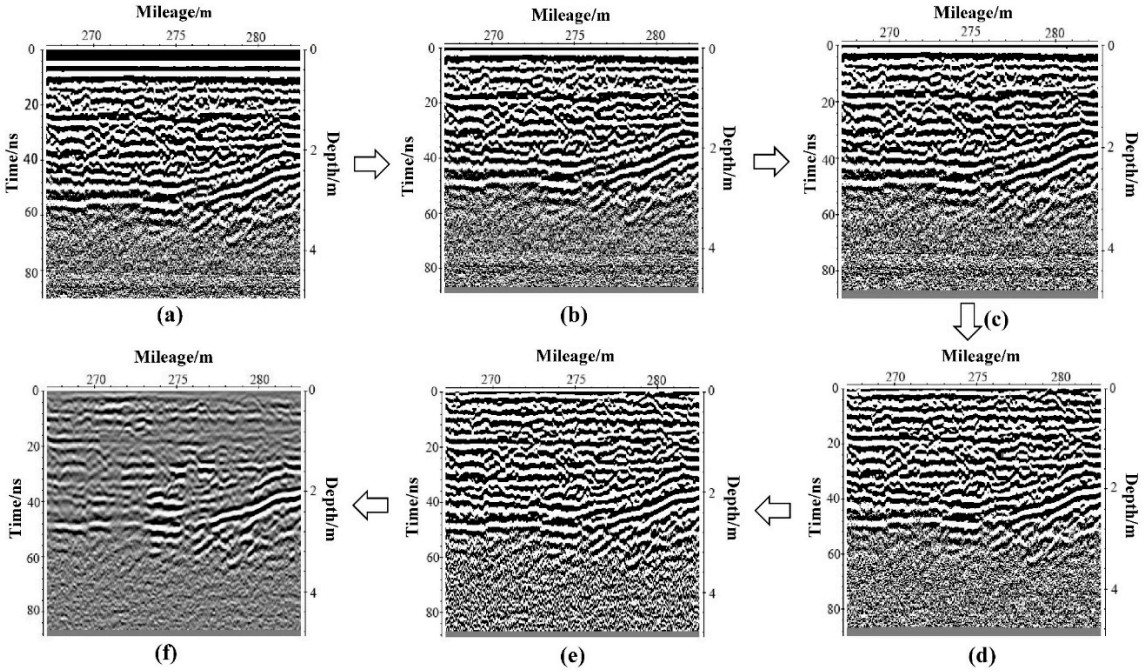

Figure 7. GPR data processing flow: (**a**) input data; (**b**) remove direct waves; (**c**) exponential gain; (**d**) average path extraction; (**e**) 1-D filtering; (**f**) 2-D filtering.

The radargrams were presented in the form of two-dimensional images. The horizontal axis was determined by highway mileage. The left-hand vertical axis shows the two-way travel time of the electromagnetic signal. The right-hand vertical axis converts the time to depth using $v = 0.11$ m/ns.

3.4. GPR Data Interpretation

The interpretation of GPR data not only needs to understand all aspects of data acquisition and processing, but also needs to combine other data and methods. In addition, due to the clear structure and materials of the block-stone embankment, it can focus more effort on the abnormal changes of different layers when interpreting the GPR data, which greatly reduces the difficulty. Therefore, the interpretation of GPR data is based on the following points: (1) field survey data, (2) effective permittivity and wave velocity, (3) reflection coefficient, (4) attenuation, and (5) GPR data analogy.

3.4.1. Field Survey Data

Detailed pavement damages, repairs, cracks, and whether the embankment settlement and block-stone layers are blocked and weathered, can provide important references for the interpretation. The condition of the embankment can directly reflect the occurrence and degree of the damage, so for the GPR data, the interpretation should consider whether or not the embankment settlement occurred in reality in the block-stone layer settlement. In addition, the environmental factors, such as vegetation conditions around the highway and thermokarst lakes, should also be fully considered.

3.4.2. Effective Permittivity and Wave Velocity

The damages to the sand-gravel and block-stone layers, whether loose or dense, will cause changes in their electrical parameters, which are largely caused by the changes in the air volume. Therefore, the Rayleigh model [72,73] introduces the calculated effective permittivity of the mixed medium, which is generally considered to be a function of the permittivity of each component and its volume content, and it can be calculated from

$$\frac{\varepsilon_{eff} - \varepsilon_1}{\varepsilon_{eff} + 2\varepsilon_1} = f\frac{\varepsilon_2 - \varepsilon_1}{\varepsilon_2 + 2\varepsilon_1} \tag{3}$$

where ε_1 and ε_2 represent the dielectric constant of the matrix medium and air in the mixture, respectively, ε_{eff} is the dielectric constant of the two-phase mixture, and f is the volume fraction of air in the mixed medium. According to the Rayleigh model, as the volume of air increases from the mixed medium, the effective permittivity will decrease, and the wave velocity will increase. Since the radargrams convert the time to the depth at a certain velocity, the increase or decrease in the wave velocity makes the same layer of the radargrams locally elongated or shortened. We need to pay attention to such changes in GPR data interpretation.

3.4.3. Reflection Coefficient

A component of the propagating GPR waves are reflected when they encounter layers composed of different mediums. The strength of the reflection from two mediums is expressed as the reflection coefficient R calculated from

$$R = \frac{\sqrt{\varepsilon_1} - \sqrt{\varepsilon_2}}{\sqrt{\varepsilon_1} + \sqrt{\varepsilon_2}} \tag{4}$$

where ε_1 and ε_2 are the dielectric constants of the medium. According to the reflection coefficient, the reflection is more obvious when the difference in the dielectric constants of the two layers is larger. (Figure 5c,d). In addition, when $R > 0$, the phase of the interface reflection wave is the same as that of the incident wave. When $R < 0$, the phase of the interface reflection wave is opposite to that of the incident wave [69].

The block-stone embankment is composed of multiple layers which are made up of different mediums, and the dielectric constant of each layer is also different. Therefore, different layers can be divided by the reflection of electromagnetic waves. A strong reflection interface, which will generate multiples, will be generated due to the large difference in the dielectric constant between the air and the block-stone. The generation of multiples is also an important method to recognize the block-stone layer.

3.4.4. Attenuation

GPR was used in the lossy medium which can cause signal attenuation. The attenuation of electromagnetic waves is related to the conductivity, dielectric, frequency scattering, and geometric spreading losses of the medium. The loss tangent, which measures the loss characteristics, can be calculated from [68]

$$tan\delta = \frac{\sigma}{\omega\varepsilon} \tag{5}$$

where δ is the loss angle, σ is the conductivity of a medium (S/m), ω is the angular frequency (rad/s), and ε is the permittivity (F/m).

In general, the air is a lossless medium, and another medium, whether a base course or a block-stone layer, will cause the attenuation of electromagnetic waves. Therefore, when the sand-gravel layer or the block-stone layer becomes loose, its attenuation will decrease. On the contrary, when the block-stone layer becomes dense, its attenuation will increase. This is also one of the methods to judge the abnormality of the sand-gravel layers and block-stone layers.

3.4.5. GPR Data Analogy

The comparison of GPR profile characteristics in similar studies is also an important method of GPR data interpretation, especially when there is a lack of certain data or controversy over the interpretation of the targets, and a comparison with previous research results can help us make judgments.

4. Results

4.1. Interpreted Results of GPR Profiles

Based on the structural characteristics of the block-stone embankment and the GPR data interpretation methods in 3.4, the damages were divided into: loosening of the upper sand-gravel layer; loosening of the block-stone layer; settlement of the block-stone layer; and dense filling of block-stone layer.

4.1.1. Loosening of the Upper Sand-Gravel Layer

Figure 8 shows the GPR images of the loosening of the upper sand-gravel layer at several different locations, and the sand-gravel layers were located at a depth of about 0.4–0.8 m. Figure 8a,b, and c all show the local weakening of the reflections at depths around 0.8-m (yellow dashed box), which was due to the damage of the geotextile. The damaged geotextile caused the upper sand-gravel to fall into the block-stone layer, which has been well-documented, and the low reflection area appeared in the block-stone layer (depth of about 0.8–2.2 m) in Figure 8c, which was the reason. From the analysis of the parameters of the GPR profile, the waveform showed low-frequency oscillation without a local strong amplitude, which was different from the waveform in the surrounding area. In general, the main reason for the loosening of the upper sand-gravel was the damage of the geotextile, which made the sand-gravel layer lack constraints.

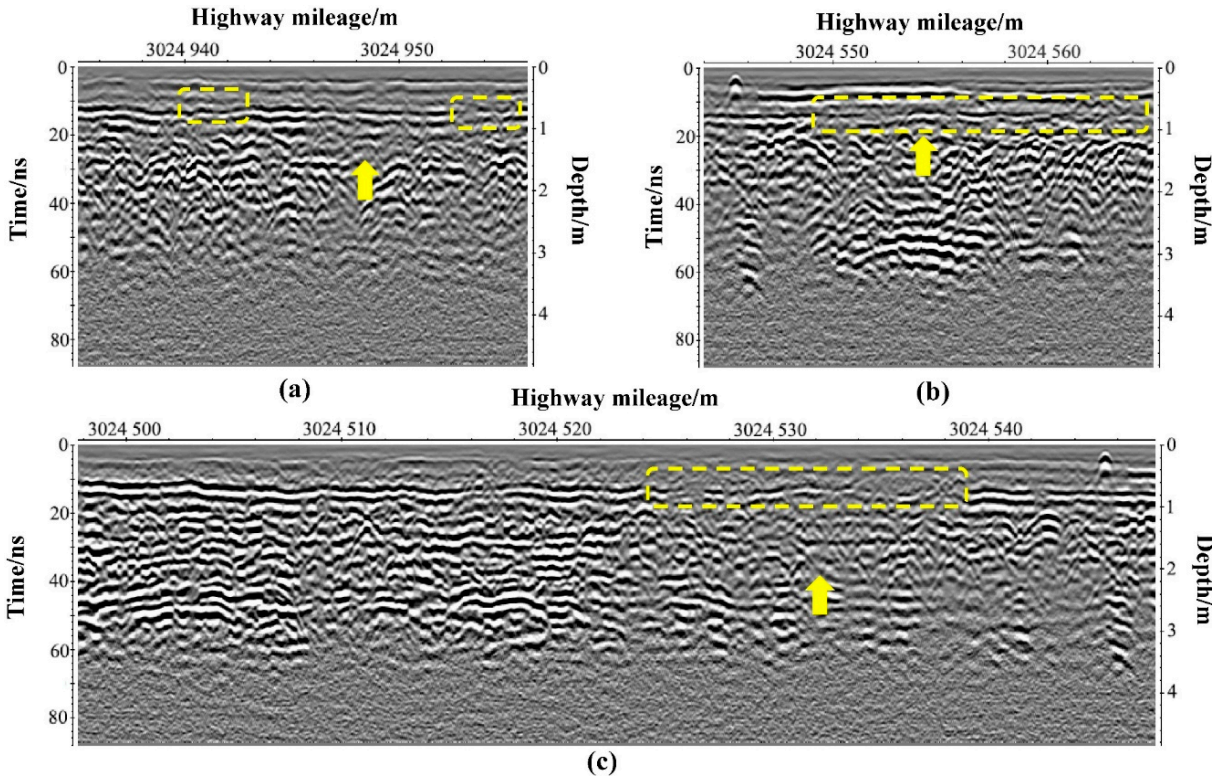

Figure 8. GPR images of the loosening of the upper sand-gravel layers: (**a**) K3024 + 935 to K3024 + 956; (**b**) K3024 + 544 to K3024 + 565; and (**c**) K3024 + 498 to K3024 + 548. The yellow dashed box shows the abnormal area of the sand-gravel layer, and the yellow arrow is used to facilitate reading.

4.1.2. Loosening of the Block-Stone Layer

Figure 9 shows two GPR images with the loosening of the block-stone layers, with a depth of about 0.8–2.4 m, which were mainly manifested as disordered electromagnetic waveforms in the block-stone layers, with a large number of short, discontinuous, and irregularly arranged reflections. This was significantly different from the GPR profile of the regularly arranged block-stone layers [74]. An abnormal signal was seen in the lower part of the block-stone layer (Figure 9a,b, red dashed box) of a strong reflection, and the amplitude increased significantly and was located in the abnormal area under the embankment, which may have been the reason leading to the loosening of the block-stone layer.

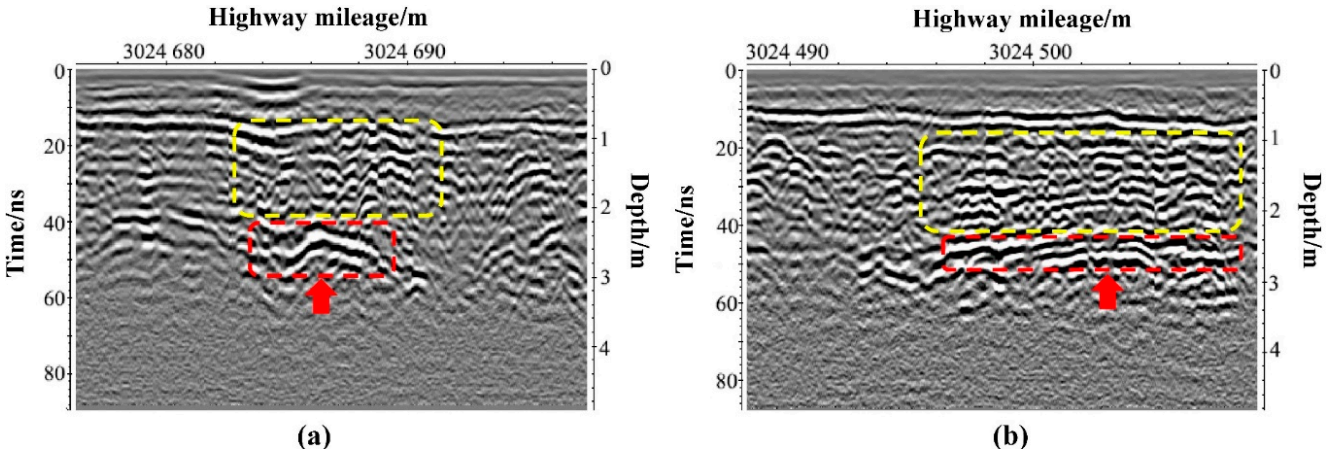

Figure 9. GPR images indicating looseness of the block-stone layers: (**a**) K3024 + 676 to K3024 + 697; (**b**) K3024 + 488 to K3024 + 509. The yellow dashed box shows the abnormal area of the block-stone layer, the red dashed box shows the abnormal area of the ground, and the yellow and red arrow is used to facilitate reading.

4.1.3. Settlement of the Block-Stone Layer

Figure 10 shows the GPR images of the block-stone layer at two locations, indicating the settlement of the block-stone layer. Figure 10a shows that the block-stone layer settled from a depth of 0.8-m on the left-hand side to a depth of 1.2-m on the right-hand side, and the sand-gravel layer also became loose with the settlement, and the geotextile was damaged on the right-hand side (yellow dashed box). Figure 10b shows that the whole block-stone layer had a settlement of about 0.2–0.4 m compared with other locations, and the settlement in the middle part was the largest. This settlement will lead to the loosening or settlement of the upper layers of the block-stone layer, which was also represented in the waveform diagram. Two irregular stone layers will be formed. The "wave" pavement will form due to these two irregular block-stone layer settlements (Figure 2c).

4.1.4. Dense Filling of Block-Stone Layer

Figure 11 shows the GPR images of the dense filling of the block-stone layer. The most notable feature is the large area of low reflection (yellow dashed box). The sand-gravel layer in both figures was abnormal, especially in Figure 11b. It is difficult to directly observe this layer in the GPR image. Only the embankment structure and GPR parameters (wave velocity, waveform, etc.) can determine the existence of this layer (shown by the red dotted line, with the bottom at a depth of about 1-m). In addition, the electromagnetic wave Rao arc generated by the block-stone was visible in the radar image.

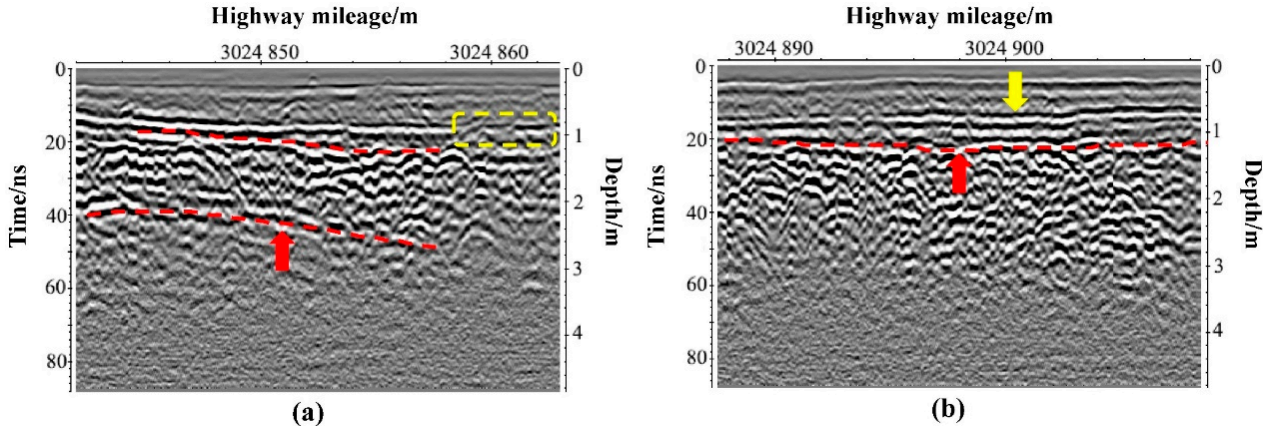

Figure 10. GPR images indicating the settlement of the block-stone layer: (**a**) K3024 + 842 to K3024 + 863; (**b**) K3024 + 887 to K3024 + 909. The yellow dashed box shows the abnormal area of the sand-gravel layer, the red dotted line indicates the settlement trend of the block-stone layer, and the yellow and red arrow is used to facilitate reading.

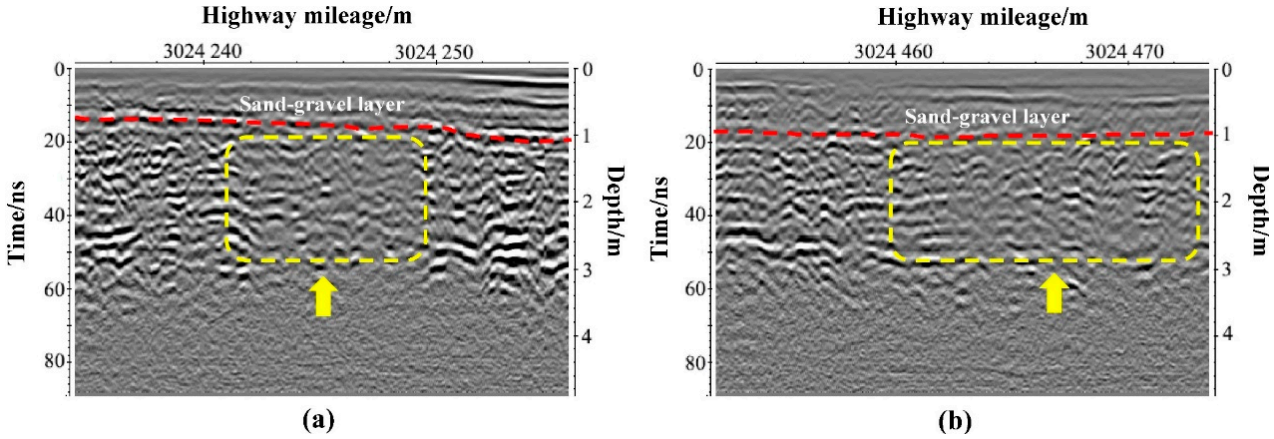

Figure 11. GPR images of an abnormally dense block-stone layer: (**a**) K 3024 + 235 to K3024 + 256; (**b**) K 3024 + 452 to K3024 + 474. The yellow dashed box shows the abnormal area of the block-stone layer, the red dotted line indicates the boundary between the sand-gravel layer and the block-stone layer, and the yellow arrow is used to facilitate reading.

GPR images cannot exhibit low reflections due to the different data processing steps, which are verified as follows (Figure 12). Figure 12a is an image processed according to the normal steps. In Figure 12b, only gain processing was performed on the image after direct wave removal. In Figure 12c, only horizontal signals were removed based on the last step. In Figure 12d, only moving-average processing was performed based on the last step. These results show that the different processing steps did not affect the results.

4.2. Distribution of Damages to the Block-Stone Embankment

The distribution of different types of damage, the overall condition of the embankment, and the relationship between various damages were studied in the K3024 to K3025 section of the block-stone embankment to further study the damage properties.

Figure 13 shows the basic properties of the embankment damage in the study section. Figure 13a shows the distribution of different types of damage. Loosening of the upper sand-gravel layer occurred most frequently. The densely filled block-stone layer occurred the least. The overall properties of the damage in the study section (Figure 13b) indicated that the damage ratio in this section was high, and the highway condition was poor.

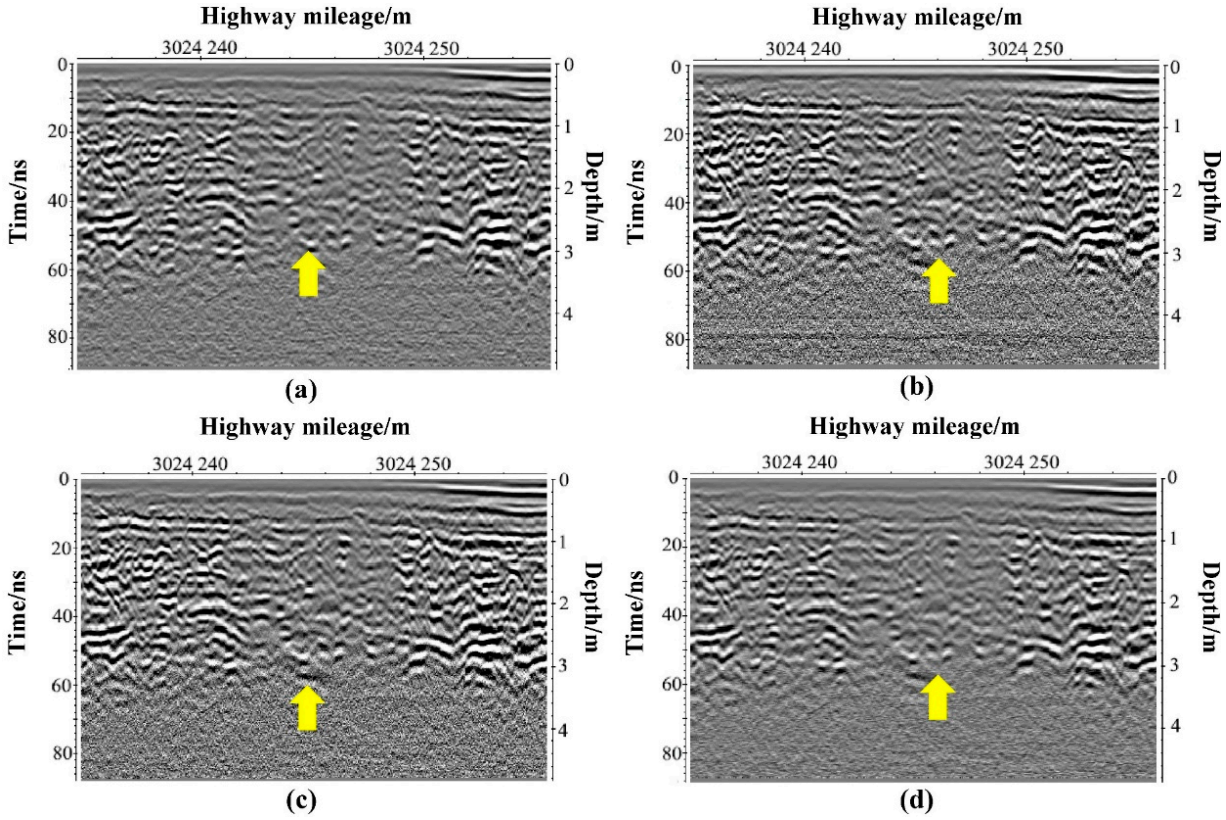

Figure 12. Comparison of the results of different processing methods for abnormally dense areas: (**a**) processed according to the normal flow; (**b**) after direct wave removal only gain processing was performed; (**c**) only horizontal signals were removed based on the previous step; (**d**) only moving-average processing was performed based on the previous step. The yellow arrow is used to increase visibility.

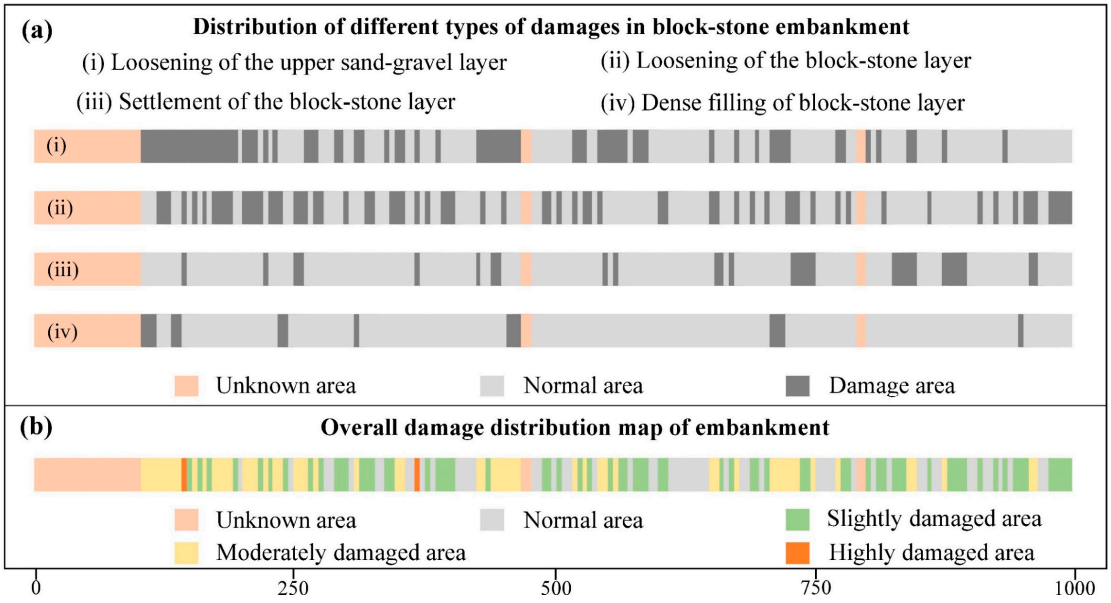

Figure 13. For the K3024 to K3025 section: (**a**) distribution of different types of damage in the block-stone embankment. Note: the unit (five meters as a unit) was considered damaged if the unit was damaged more than half, otherwise, it was a normal unit. (**b**) overall damage situation of the embankment. Note: The degree of embankment damage was based on the number of damaged species on each unit.

Figure 14 shows the distribution length of the different types of damage and the relationships between them. Figure 14a shows the damage length and damage ratio of the different types of damages. The damage of the loosening of the upper sand-gravel layer was the longest one, accounting for 40.9%. The damage of the dense filling of the block-stone layer was the shortest one, accounting for 7.39%. Figure 14b shows the length and proportion of highway sections with different damage ratios. The proportions of the normal area, slightly damaged area, and moderately damaged area were similar, accounting for 32.38%, 35.2%, and 31.25%, respectively. The proportions of the highly damaged area were equal, accounting for 1.14% of the study section.

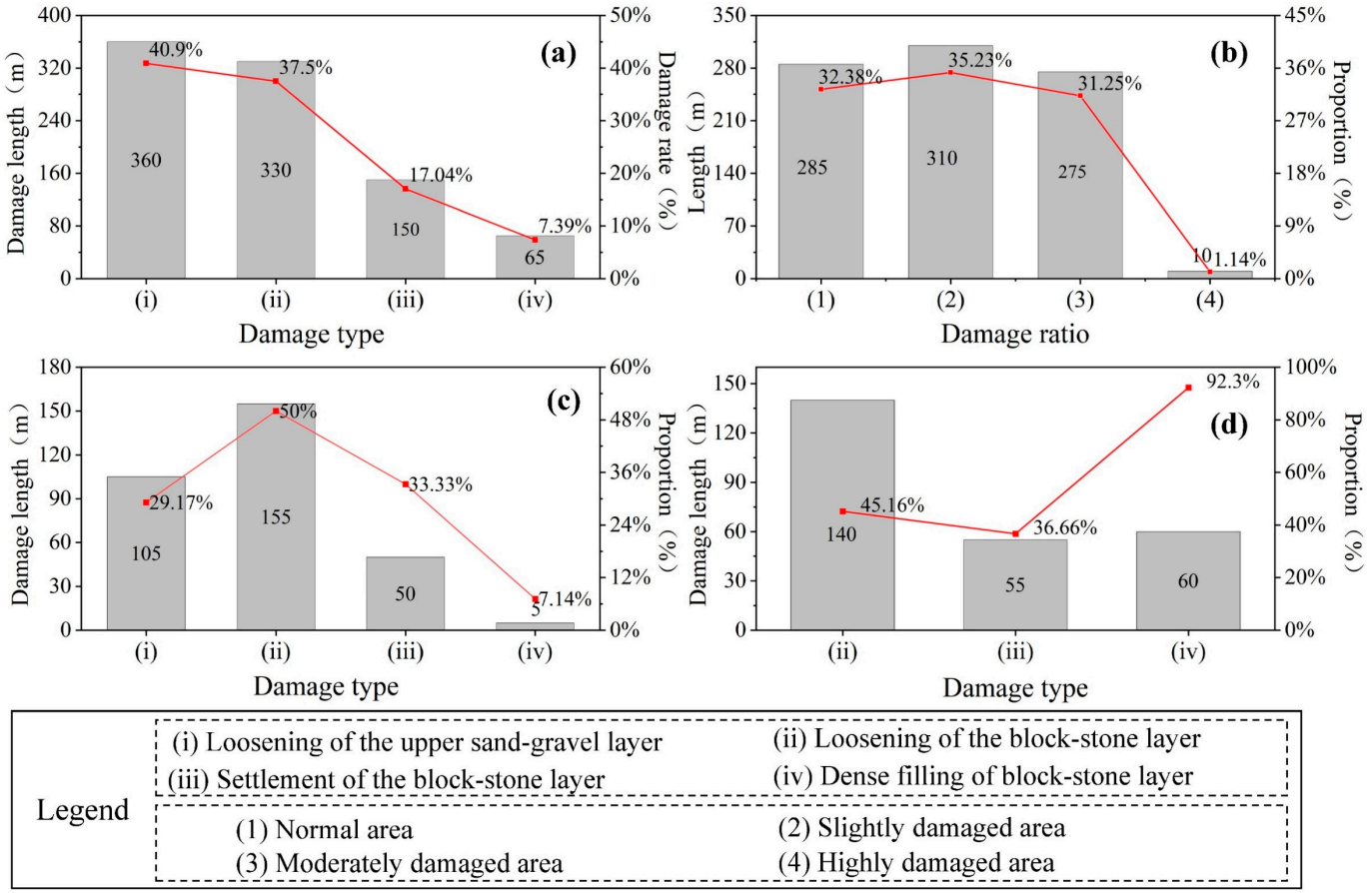

Figure 14. Relationship of different types of damage in the block-stone embankment: (**a**) shows the damaged length and rate of the different types of damage; (**b**) shows the length and proportion of highway sections with different degrees of damage; (**c**) shows the relationship between the different types of damage and the abnormality of the lower part of the embankment; (**d**) shows the relationship between the different types of damage and the loosening of the upper sand-gravel layer.

Figure 14c shows the relationship between the different types of damage and the anomaly of GPR images in the lower part (indicated by the red arrow in Figure 9) of the embankment. The damage of the loosening of the block-stone layers was the greatest one, accounting for about half. Figure 14d shows a very high correlation (92.3%) between the loosening of the upper sand-gravel layer and the dense filling of the block-stone layer, indicating that the primary reason for the dense filling was the falling and filling of the sand-gravel.

5. Discussion

The block-stone embankment is widely used in permafrost regions. However, studies to date have mainly focused on the design and optimization of the structure of block-stone embankments [28–32], with little research on their damages. The study on its damage reasons and properties is of great significance. In this study, GPR was used to conduct a relatively complete study on these damages.

GPR is a geophysical method for revealing underground medium details utilizing the reflection and refraction of electromagnetic waves within the medium [34–36]. Different parts and types of damages on the block-stone embankment have different characteristics of GPR signals, which can be observed in GPR images. For example, Figure 8 shows that the GPR images of the loosening of the upper sand-gravel layer were mainly manifested as the local weakening of the reflections at depths around 0.8-m, and the waveform showed low-frequency oscillation without local strong amplitude. Figure 9 shows GPR images of the loosening of the block-stone layers at depths of about 0.8–2.4 m, which were mainly manifested as disordered electromagnetic waveforms in the block-stone layers, with a large number of short, discontinuous, and irregularly arranged reflections. In this way, GPR imagery, together with the other data and methods (structural characteristics, field survey data, GPR parameters, etc.), indicated categories of damages. According to the above results, the distribution of different types of damages and the overall damages of the study section can be drawn (Figure 13).

The relationship between the different damages in a block-stone embankment was highly significant. The development process and causes of damages were roughly inferred according to their relationships. For example, Figure 14b shows that 50% of the loosening of the block-stone layer was related to the abnormality of the lower part of the embankment. Figure 14d shows that 92.3% of the dense filling of the block-stone layer was related to the loosening of the upper sand-gravel layer, indicating that most of the dense filling of the block-stone layer was caused by the falling and filling of the overlying sand-gravel soil. In addition, there were complex relationships between the damages and causes. For example, the thawing settlement of the permafrost under the embankment is the first prerequisite for the damage of block-stone embankment damages. These in turn cause the deterioration of the structure and function of the block-stone embankment, which leads to a breakdown in the engineering conditions of the permafrost beneath the embankment, thus completing a vicious cycle.

Based on the above research, this study has revealed a preliminary account of the formation processes of the damages (Figure 15), which are more complex and diverse in practice than the following simplified description. Figure 15a shows that the action of various influencing factors caused the thawing of the permafrost beneath the block-stone embankment, creating the hidden danger of embankment instability. Figure 15b shows that active layer changes affected the embankment, which was mainly manifested as the local loosening of the block-stone layer and local damage to the top sand-gravel layer, and partial longitudinal cracks then appeared on the pavement. These changes were exacerbated by the rolling action of vehicles on the damaged highway embankment. Figure 15c shows the worsening damage to the embankment as the block-stone layer was loosened in many places, and some of the block stones settled with the settlement of the embankment, further accelerating the local fragmentation of the top sand-gravel layer, with some of the material falling into the block-stone layer. The number and width of longitudinal cracks on the pavement increased, and transverse cracks began to appear [75]. Figure 15d shows that the interlayer space between each structural layer was further enlarged as the damage progressed, the cracks in the asphalt pavement further increased, and the embankment structure was greatly damaged. In addition, the uneven settlement of the embankment formed a “wavy” pavement, which severely affected the safety and comfortability of driving.

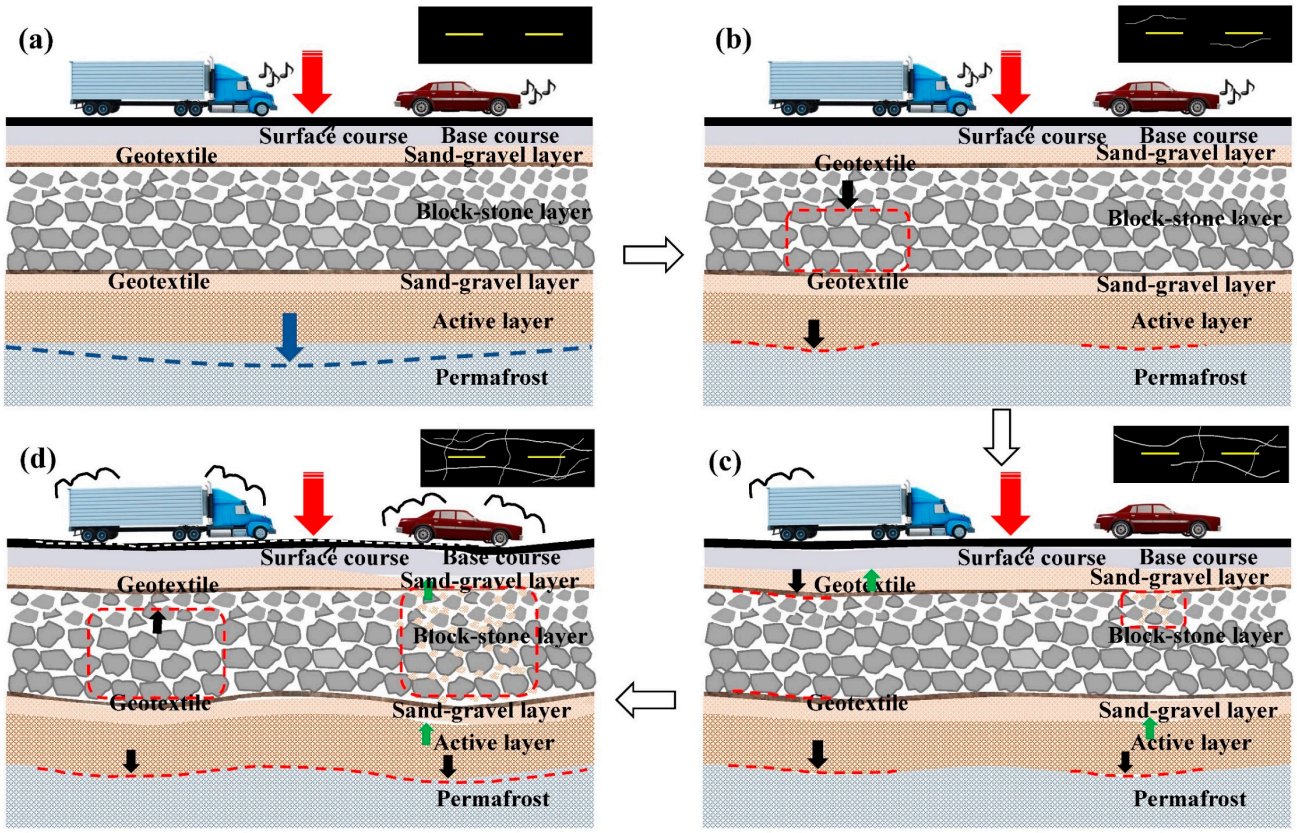

Figure 15. Progressive formation of block-stone embankment damage: (**a**) shows that the action of various influencing factors causes the thawing of the permafrost beneath the embankment; (**b**) shows the active layer changes that affected the embankment; (**c**) shows the worsening damage to the embankment; (**d**) shows that as the damage progressed, the embankment structure was greatly damaged. The red arrows indicate the influence of the external environment on the embankment (such as sun exposure and vehicle rolling), and the other dotted boxes and arrows are used to facilitate reading.

6. Conclusions

This study investigated the types, distribution, formation processes, and influencing factors of damage to block-stone embankments and their relationships using GPR imagery. The findings of the study led to the following conclusions:

(1) GPR efficiently and quickly detected and identified the damages in the study area of the block-stone embankment. Four categories of damage were determined: (i) loosening of the upper sand-gravel layer; (ii) loosening of the block-stone layer; (iii) settlement of the block-stone layer; and (iv) dense filling of the block-stone layer. Of these, (i) and (ii) were widely distributed, but (iii) and (iv) less so;

(2) Due to the complex structure of the block-stone embankment, in particular the block-stone layer itself, the attenuation of the electromagnetic wave signals was more noticeable than in the other embankment materials. Therefore, it was difficult to detect and study the deeper parts of the embankment. The quality of GPR data processing also played a very important role in image interpretation;

(3) Loosening of the sand-gravel layer was found to be the most widely distributed, and the least was the dense filling of the block-stone layer. However, the primary reason for the dense filling of the block-stone layer was the falling of the overlying sand-gravel soil. The studied section of the embankment was in the primary stage of deterioration. With further development of the damage, more of the block-stone layers will be filled with sand gravel soil;

(4) The formation of block-stone embankment damages is a complex process resulting from various factors that have close relationships with each other. The block-stone layer was put in the highway embankment to protect the underlying permafrost from the thaw. Once the damage occurs in the block stone embankment, it will weaken its cooling effect leading to worse damages.

Author Contributions: Conceptualization, S.Q., G.L., M.C. and D.C.; methodology, S.Q., M.C. and G.L.; validation, S.Q., G.L., D.C., Y.Z. and Q.D.; formal analysis, S.Q., G.L., D.C., Y.Z. and Q.D.; investigation, S.Q., G.L., D.C. and Q.D.; data curation, S.Q., G.L. and D.C.; writing—original draft preparation, S.Q. and G.L.; writing—review and editing, S.Q. and G.L.; visualization, S.Q. and G.L.; supervision, D.C., Y.Z., Q.D., G.L., M.C., Y.C., L.T. and H.J.; project administration, G.L., Y.C., L.T. and H.J.; funding acquisition, G.L. and D.C. All authors have read and agreed to the published version of the manuscript.

Funding: This research was funded by the Second Tibetan Plateau Scientific Expedition and Research Program (No.2019QZKK0905), the National Natural Science Foundation of China (No. U1703244), the Foundation of the State Key Laboratory of Frozen Soil Engineering (No. SKLFSE-ZY-20), the Foundation of the State Key Laboratory for Geomechanics and Deep Underground Engineering (No. SKLGDUEK 1904).

Data Availability Statement: Not applicable.

Acknowledgments: The data set in Figure 2a is provided by National Tibetan Plateau Data Center (http://data.tpdc.ac.cn). The authors especially thank Peifeng He and Jing Luo for their field assistance and Yan Zhang for his help with Figure 13.

Conflicts of Interest: The authors declare no conflict of interest.

References

1. Yu, S.; Zhang, J.; Liu, Y.; Wu, J. Thermal regime in the embankment of Qinghai–Tibetan Highway in permafrost regions. *Cold Reg. Sci. Technol.* **2002**, *35*, 35–44. [CrossRef]
2. Nelson, F.E.; Anisimov, O.A.; Shiklomanov, N.I. Subsidence risk from thawing permafrost. *Nature* **2001**, *410*, 889–890. [CrossRef]
3. Biskaborn, B.K.; Smith, S.L.; Noetzli, J.; Matthes, H.; Vieira, G.; Streletskiy, D.A.; Schoeneich, P.; Romanovsky, V.E.; Lewkowicz, A.G.; Abramov, A.; et al. Permafrost is warming at a global scale. *Nat. Commun.* **2019**, *10*, 264. [CrossRef] [PubMed]
4. Smith, S.L.; O'Neill, H.B.; Isaksen, K.; Noetzli, J.; Romanovsky, V.E. The changing thermal state of permafrost. *Nat. Rev. Earth Environ.* **2022**, *3*, 10–23. [CrossRef]
5. Zhongqiong, Z.; Qingbai, W.; Guanli, J.; Siru, G.; Ji, C.; Yongzhi, L. Changes in the permafrost temperatures from 2003 to 2015 in the Qinghai-Tibet Plateau. *Cold Reg. Sci. Technol.* **2019**, *169*, 102904. [CrossRef]
6. Yu, Q.; Fan, K.; You, Y.; Guo, L.; Yuan, C. Comparative analysis of temperature variation characteristics of permafrost roadbeds with different widths. *Cold Reg. Sci. Technol.* **2015**, *117*, 12–18. [CrossRef]
7. Yu, F.; Qi, J.; Lai, Y.; Sivasithamparam, N.; Yao, X.; Zhang, M.; Liu, Y.; Wu, G. Typical embankment settlement/heave patterns of the Qinghai–Tibet highway in permafrost regions: Formation and evolution. *Eng. Geol.* **2016**, *214*, 147–156. [CrossRef]
8. Peng, H.; Ma, W.; Mu, Y.-H.; Jin, L.; Yuan, K. Degradation characteristics of permafrost under the effect of climate warming and engineering disturbance along the Qinghai–Tibet Highway. *Nat. Hazards* **2014**, *75*, 2589–2605. [CrossRef]
9. Zhang, Z.; Wu, Q.; Xun, X. Radiation and energy balance characteristics of asphalt pavement in permafrost regions. *Environ. Earth Sci.* **2016**, *75*, 221. [CrossRef]
10. Zhang, Z.; Wu, Q.; Liu, Y.; Gao, S. Characteristics of water and heat changes in near-surface layers under influence of engineering interface. *Appl. Therm. Eng.* **2017**, *125*, 986–994. [CrossRef]
11. Zhang, Z.; Wu, Q.; Liu, Y.; Zhang, Z.; Wu, G. Thermal accumulation mechanism of asphalt pavement in permafrost regions of the Qinghai–Tibet Plateau. *Appl. Therm. Eng.* **2018**, *129*, 345–353. [CrossRef]
12. Alfaro, M.; Ciro, G.; Thiessen, K.; Ng, T. Case Study of Degrading Permafrost beneath a Road Embankment. *J. Cold Reg. Eng.* **2009**, *23*, 93–111. [CrossRef]
13. Ya-Ling, C.; Sheng, Y.; Ma, W. Study on the effect of the thermal regime differences in roadbed slopes on their thawing features in permafrost regions of Qinghai–Tibetan plateau. *Cold Reg. Sci. Technol.* **2008**, *53*, 334–345. [CrossRef]
14. O'Neill, B.; Burn, C. Impacts of variations in snow cover on permafrost stability, including simulated snow management, Dempster Highway, Peel Plateau, Northwest Territories. *Arct. Sci.* **2017**, *3*, 150–178. [CrossRef]
15. Wu, Q.; Zhang, Z.; Liu, Y. Long-term thermal effect of asphalt pavement on permafrost under an embankment. *Cold Reg. Sci. Technol.* **2010**, *60*, 221–229. [CrossRef]
16. Ma, W.; Mu, Y.; Wu, Q.; Sun, Z.; Liu, Y. Characteristics and mechanisms of embankment deformation along the Qinghai–Tibet Railway in permafrost regions. *Cold Reg. Sci. Technol.* **2011**, *67*, 178–186. [CrossRef]

17. Wang, S.; Niu, F.; Chen, J.; Dong, Y. Permafrost research in China related to express highway construction. *Permafr. Periglac.* **2020**, *31*, 406–416. [CrossRef]
18. Fan, K. Study on Design and Construction techniques of Special Subgrade for Permafrost Areas. Master's Thesis, Chang'an University, Xi'an, China, 2009.
19. Doré, G.; Niu, F.; Brooks, H. Adaptation Methods for Transportation Infrastructure Built on Degrading Permafrost. *Permafr. Periglac.* **2016**, *27*, 352–364. [CrossRef]
20. Zhi, W.; Yu, S.; Wei, M.; Jilin, Q. Evaluation of EPS application to embankment of Qinghai–Tibetan railway. *Cold Reg. Sci. Technol.* **2005**, *41*, 235–247. [CrossRef]
21. Qin, Y.; Zhang, J. A review on the cooling effect of duct-ventilated embankments in China. *Cold Reg. Sci. Technol.* **2013**, *95*, 1–10. [CrossRef]
22. Wang, S.; Li, Z.; Zhang, J.; Chen, J. *Highway Construction Technology on Permafrost Regions*; China Communications Press: Beijing, China, 2008; pp. 25–32.
23. Cheng, G.; Wu, Q.; Ma, W. Innovative designs of permafrost roadbed for the Qinghai-Tibet Railway. *Sci. China Ser. E Technol. Sci.* **2009**, *52*, 530–538. [CrossRef]
24. Fang, J.; Li, D.; Xu, A.; Tong, C. *Application Technology of Special Subgrade Engineering Measures in Permafrost Regions*; Lanzhou University Press: Lanzhou, China, 2016; pp. 25–32.
25. Mu, Y.; Ma, W.; Liu, Y.; Sun, Z. Monitoring investigation on thermal stability of air-convection crushed-rock embankment. *Cold Reg. Sci. Technol.* **2010**, *62*, 160–172. [CrossRef]
26. Xi, J.; Zhang, S.; Chen, J.; Jin, L.; Dong, Y. Analysis of the Cooling Effect of Block Stone Embankment at Wudaoliang Section of the Qinghai-Tibet Highway. *China J. Highw. Transport.* **2014**, *27*, 17–23. [CrossRef]
27. Liu, M.; Li, G.; Niu, F.; Lin, Z.; Shang, Y. Porosity of crushed rock layer and its impact on thermal regime of Qinghai−Tibet Railway embankment. *J. Cent. South Univ.* **2017**, *24*, 977–987. [CrossRef]
28. Liu, M.; Niu, F.; Ma, W.; Fang, J.; Lin, Z.; Luo, J. Experimental investigation on the enhanced cooling performance of a new crushed-rock revetment embankment in warm permafrost regions. *Appl. Therm. Eng.* **2017**, *120*, 121–129. [CrossRef]
29. Liu, M.; Niu, F.; Luo, J.; Yin, G.; Zhang, L. Performance, applicability, and optimization of a new slope cooling and protection structure for road embankment over warm permafrost. *Int. J. Heat Mass Transf.* **2020**, *162*, 120388. [CrossRef]
30. Zhang, M.; Lai, Y.; Li, S.; Zhang, S. Laboratory investigation on cooling effect of sloped crushed-rock revetment in permafrost regions. *Cold Reg. Sci. Technol.* **2006**, *46*, 27–35. [CrossRef]
31. Qian, J.; Yu, Q.; Guo, L.; Hu, J. Experimental study on convection characteristics of crushed-rock layer. *Can. Geotech. J.* **2013**, *50*, 834–840. [CrossRef]
32. Lai, Y.; Ma, W.; Zhang, M.; Yu, W.; Gao, Z. Experimental investigation on influence of boundary conditions on cooling effect and mechanism of crushed-rock layers. *Cold Reg. Sci. Technol.* **2006**, *45*, 114–121. [CrossRef]
33. Wang, S.; Xiong, L.; Zhang, C.; Mu, K.; Jin, L. Fuzzy expert prediction method for highway diseases in permafrost region. *J. Traffic Transp. Eng.* **2016**, *16*, 112–121. [CrossRef]
34. Davis, J.L.; Annan, A.P. Ground-Penetrating Radar for High-Resolution Mapping of Soil and Rock STRATIGRAPHY1. *Geophys. Prospect.* **1989**, *37*, 531–551. [CrossRef]
35. Blindow, N. Ground Penetrating Radar. In *Groundwater Geophysics: A Tool for Hydrogeology*; Kirsch, R., Ed.; Springer: Berlin/Heidelberg, Germany, 2006; pp. 227–252.
36. Liu, L.; Qian, R. Ground penetrating radar: A critical tool in near-surface geophysics. *Chin. J. Geophys.* **2015**, *58*, 2606–2617. [CrossRef]
37. Núñez-Nieto, X.; Solla, M.; Gómez-Pérez, P.; Lorenzo, H. GPR Signal Characterization for Automated Landmine and UXO Detection Based on Machine Learning Techniques. *Remote Sens.* **2014**, *6*, 9729–9748. [CrossRef]
38. Abouhamad, M.; Dawood, T.; Jabri, A.; Alsharqawi, M.; Zayed, T. Corrosiveness Mapping of Bridge Decks Using Image-Based Analysis of GPR Data. *Autom. Constr.* **2017**, *80*, 104–117. [CrossRef]
39. Zhang, F.; Xie, X.; Huang, H. Application of ground penetrating radar in grouting evaluation for shield tunnel construction. *Tunn. Undergr. Space Technol.* **2010**, *25*, 99–107. [CrossRef]
40. Diallo, M.; Cheng, L.; Rosa, E.; Gunther, C.; Chouteau, M. Integrated GPR and ERT data interpretation for bedrock identification at Cléricy, Québec, Canada. *Eng. Geol.* **2018**, *248*, 230–241. [CrossRef]
41. Pilecki, Z.; Krzysztof, K.; Elżbieta, P.; Andrzej, K.; Sylwia, T.-S.; Tomasz, Ł. Identification of buried historical mineshaft using ground-penetrating radar. *Eng. Geol.* **2021**, *294*, 106400. [CrossRef]
42. Iftimie, N.; Savin, A.; Steigmann, R.; Dobrescu, G.S. Underground Pipeline Identification into a Non-Destructive Case Study Based on Ground-Penetrating Radar Imaging. *Remote Sens.* **2021**, *13*, 3494. [CrossRef]
43. Forte, E.; Pipan, M.; Casabianca, D.; Di Cuia, R.; Riva, A. Imaging and characterization of a carbonate hydrocarbon reservoir analogue using GPR attributes. *J. Appl. Geophys.* **2012**, *81*, 76–87. [CrossRef]
44. Alani, A.M.; Aboutalebi, M.; Kilic, G. Applications of ground penetrating radar (GPR) in bridge deck monitoring and assessment. *J. Appl. Geophys.* **2013**, *97*, 45–54. [CrossRef]
45. Zhao, W.; Forte, E.; Pipan, M.; Tian, G. Ground Penetrating Radar (GPR) attribute analysis for archaeological prospection. *J. Appl. Geophys.* **2013**, *97*, 107–117. [CrossRef]

46. Hughes, L.J. Mapping contaminant-transport structures in karst bedrock with ground-penetrating radar. *Geophysics* **2009**, *74*, B197–B208. [CrossRef]
47. Solla, M.; Pérez-Gracia, V.; Fontul, S. A Review of GPR Application on Transport Infrastructures: Troubleshooting and Best Practices. *Remote Sens.* **2021**, *13*, 672. [CrossRef]
48. Peng, S.; Yang, F.; Xu, X. Application and Prospects of the GPR Technology on Road Damage Detection in China. In Proceedings of the Near-Surface Asia Pacific Conference, Waikoloa, Hawaii, 7–10 July 2015; pp. 476–479.
49. Krysiński, L.; Sudyka, J. GPR abilities in investigation of the pavement transversal cracks. *J. Appl. Geophys.* **2013**, *97*, 27–36. [CrossRef]
50. Liu, G.; Zhao, L.; Xie, C.; Zou, D.; Wu, T.; Du, E.; Wang, L.; Sheng, Y.; Zhao, Y.; Xiao, Y.; et al. The Zonation of Mountain Frozen Ground under Aspect Adjustment Revealed by Ground-Penetrating Radar Survey—A Case Study of a Small Catchment in the Upper Reaches of the Yellow River, Northeastern Qinghai–Tibet Plateau. *Remote Sens.* **2022**, *14*, 2450. [CrossRef]
51. Munroe, J.S.; Doolittle, J.A.; Kanevskiy, M.Z.; Hinkel, K.M.; Nelson, F.E.; Jones, B.M.; Shur, Y.; Kimble, J.M. Application of ground-penetrating radar imagery for three-dimensional visualisation of near-surface structures in ice-rich permafrost, Barrow, Alaska. *Permafr. Periglac.* **2007**, *18*, 309–321. [CrossRef]
52. Luo, J.; Niu, F.-J.; Lin, Z.-J.; Liu, M.-H.; Yin, G.-A. Variations in the northern permafrost boundary over the last four decades in the Xidatan region, Qinghai–Tibet Plateau. *J. Mt. Sci. Eng.* **2018**, *15*, 765–778. [CrossRef]
53. Sjöberg, Y.; Marklund, P.; Pettersson, R.; Lyon, S.W. Geophysical mapping of palsa peatland permafrost. *Cryosphere* **2015**, *9*, 465–478. [CrossRef]
54. Wang, Q.; Shen, Y. Calculation and Interpretation of Ground Penetrating Radar for Temperature and Relative Water Content of Seasonal Permafrost in Qinghai-Tibet Platea. *Electronics* **2019**, *8*, 731. [CrossRef]
55. Du, E.; Zhao, L.; Wu, T.; Li, R.; Yue, G.; Wu, X.; Li, W.; Jiao, Y.; Hu, G.; Qiao, Y.; et al. The relationship between the ground surface layer permittivity and active-layer thawing depth in a Qinghai–Tibetan Plateau permafrost area. *Cold Reg. Sci. Technol.* **2016**, *126*, 55–60. [CrossRef]
56. Stephani, E.; Fortier, D.; Shur, Y.; Fortier, R.; Doré, G. A geosystems approach to permafrost investigations for engineering applications, an example from a road stabilization experiment, Beaver Creek, Yukon, Canada. *Cold Reg. Sci. Technol.* **2014**, *100*, 20–35. [CrossRef]
57. Shen, Y.; Zuo, R.; Liu, J.; Tian, Y.; Wang, Q. Characterization and evaluation of permafrost thawing using GPR attributes in the Qinghai-Tibet Plateau. *Cold Reg. Sci. Technol.* **2018**, *151*, 302–313. [CrossRef]
58. Xiao, J.; Liu, L. Permafrost Subgrade Condition Assessment Using Extrapolation by Deterministic Deconvolution on Multifrequency GPR Data Acquired Along the Qinghai-Tibet Railway. *IEEE J. Sel. Top. Appl. Earth Obs. Remote Sens.* **2016**, *9*, 83–90. [CrossRef]
59. Wang, Y.; Jin, H.; Li, G. Investigation of the freeze–thaw states of foundation soils in permafrost areas along the China–Russia Crude Oil Pipeline (CRCOP) route using ground-penetrating radar (GPR). *Cold Reg. Sci. Technol.* **2016**, *126*, 10–21. [CrossRef]
60. Jørgensen, A.S.; Andreasen, F. Mapping of permafrost surface using ground-penetrating radar at Kangerlussuaq Airport, western Greenland. *Cold Reg. Sci. Technol.* **2007**, *48*, 64–72. [CrossRef]
61. Zou, D.; Zhao, L.; Sheng, Y.; Chen, J.; Hu, G.; Wu, T.; Wu, J.; Xie, C.; Wu, X.; Pang, Q.; et al. A new map of permafrost distribution on the Tibetan Plateau. *Cryosphere* **2017**, *11*, 2527–2542. [CrossRef]
62. Lin, Z. A new map of permafrost distribution on the Tibetan Plateau (2017). *Cryosphere* **2019**, *11*, 2527–2542. [CrossRef]
63. Cheng, G.; Zhao, L.; Li, R.; Wu, X.; Sheng, Y.; Hu, G.; Zhou, D.; Jin, H.; Li, X.; Wu, Q. Characteristic, changes and impacts of permafrost on Qinghai-Tibet Plateau. *Chin. Sci. Bull.* **2019**, *64*, 2783–2795. [CrossRef]
64. Wu, Q.; Zhang, Z.; Liu, G. Relationships between climate warming and engineering stability of permafrost on Qinghai-Tibet plateau. *J. Eng. Geol.* **2021**, *29*, 342–352. [CrossRef]
65. Wang, S.; Wang, Z.; Yuan, K.; Zhao, Y. Qinghai-Tibet Highway Engineering Geology in Permafrost Regions: Review and Prospect. *China J. Highw. Transp.* **2015**, *28*, 9. [CrossRef]
66. Song, Z. Study on the Adaptability of Block-Rock-Embankment in Permafrost Regions. Master's Thesis, Beijing Jiaotong University, Beijing, China, 2012.
67. Lai, Y.M.; Zhang, M.Y.; Li, S.Y. *Theory and Application of Cold Regions Engineering*; Science Press: Beijing, China, 2009; pp. 43–92.
68. Zeng, Z.F.; Liu, S.X.; Wang, Z.J.; Xue, J. *Principle and Application of Ground-Penetrating Radar*; Science Press: Beijing, China, 2006; 119p.
69. Benedetto, A.; Tosti, F.; Ciampoli, L.B.; D'Amico, F. An overview of ground-penetrating radar signal processing techniques for road inspections. *Signal Process.* **2017**, *132*, 201–209. [CrossRef]
70. Shu, Z.L.; Liu, B.X.; Liu, X.R.; Zhu, C.H. *Forward and Inverse Theory and Signal Processing of Ground-Penetrating Radar*; Science Press: Beijing, China, 2017; pp. 1–10.
71. Reflexw. *User Guide of Reflexw Computer Program*; Sandmeier Geophysical Research: Karlsruhe, Germany, 2018.
72. Sihvola, A.H.; Alanen, E. Studies of mixing formulae in the complex plane. *IEEE Trans. Geosci. Remote* **1991**, *29*, 679–687. [CrossRef]
73. Shivola, A.H. Self-consistency aspects of dielectric mixing theories. *IEEE Trans. Geosci. Remote* **2002**, *27*, 403–415. [CrossRef]

74. Wei, K.; Song, X.; Zhou, S.; Zhang, H. Characteristics of ground-penetrating radar response to abnormal defects of road gravel cushion. *J. Hohai. Univ.* **2015**, *43*, 133–138. [CrossRef]
75. Chai, M.; Li, G.; Ma, W.; Chen, D.; Du, Q.; Zhou, Y.; Qi, S.; Tang, L.; Jia, H. Damage characteristics of the Qinghai-Tibet Highway in permafrost regions based on UAV imagery. *Int. J. Pavement Eng.* **2022**, 247074867. [CrossRef]